PNAS RESEARCH ARTICLE | CELL BIOLOGY OPEN ACCESS

Defined extracellular matrix compositions support stiffness-insensitive cell spreading and adhesion signaling

James R. W. Conway[a,1], Aleksi Isomursu[a], Gautier Follain[a], Ville Härmä[b,c], Eva Jou-Ollé[a], Nicolas Pasquier[a], Eetu P. O. Välimäki[b], Juha K. Rantala[b,c], and Johanna Ivaska[a,d,e,f,g,1]

Edited by Joan Brugge, Harvard Medical School, Boston, MA; received March 15, 2023; accepted September 15, 2023

Integrin-dependent adhesion to the extracellular matrix (ECM) mediates mechanosensing and signaling in response to altered microenvironmental conditions. In order to provide tissue- and organ-specific cues, the ECM is composed of many different proteins that temper the mechanical properties and provide the necessary structural diversity. Despite most human tissues being soft, the prevailing view from predominantly in vitro studies is that increased stiffness triggers effective cell spreading and activation of mechanosensitive signaling pathways. To address the functional coupling of ECM composition and matrix rigidity on compliant substrates, we developed a matrix spot array system to screen cell phenotypes against different ECM mixtures on defined substrate stiffnesses at high resolution. We applied this system to both cancer and normal cells and surprisingly identified ECM mixtures that support stiffness-insensitive cell spreading on soft substrates. Employing the motor-clutch model to simulate cell adhesion on biochemically distinct soft substrates, with varying numbers of available ECM–integrin–cytoskeleton (clutch) connections, we identified conditions in which spreading would be supported on soft matrices. Combining simulations and experiments, we show that cell spreading on soft is supported by increased clutch engagement on specific ECM mixtures and even augmented by the partial inhibition of actomyosin contractility. Thus, "stiff-like" spreading on soft is determined by a balance of a cell's contractile and adhesive machinery. This provides a fundamental perspective for in vitro mechanobiology studies, identifying a mechanism through which cells spread, function, and signal effectively on soft substrates.

integrins | substrate stiffness | microcontact printing | extracellular matrix | molecular clutch

Significance

The ECM (extracellular matrix) provides an essential structural scaffold for tissue and organ functionality. Its composition and physical properties must be carefully controlled to give rise to the myriad forms taken by multicellular life. However, the mechanisms by which cells recognize distinct ECM landscapes and integrate these mechano-chemical signals remain unclear. Here, we demonstrate that ECM ligand availability and the integrin repertoire engaged jointly determine cell behavior in response to matrix rigidity. Through computational simulations and experimental validation, we propose a model whereby increasing the number of cell-matrix connections, "clutches", by providing cells with defined ECM combinations can fully support cell spreading on compliant matrices, offering insight into the mechanisms of cell behavior in soft tissues.

Multicellular organisms depend upon a complex network of extracellular matrix (ECM) components to provide a supportive scaffold for the function of organs and tissues. This network is deposited and remodeled predominantly by resident stromal cells and in turn guides stromal and epithelial cells as they respond to precise ECM compositions, modifications, stiffnesses, and architectures. The detection of different ECMs, and the ensuing downstream signaling in cells, occurs primarily through integrin adhesion receptors that coordinate cellular responses to different ligand combinations and can support both healthy and disease states (1–3). Indeed integrin–ECM adhesion signaling drives specific transcriptional responses (4, 5), and the functional significance of the ECM for tissues is exemplified by the severity of connective tissue disorders resulting from point mutations in collagens, laminin (Lam) isoforms, and fibrillin (6, 7). Similarly, many matrix components have been linked to a poorer prognosis in different cancer subtypes, including collagen VI (ColVI) (8), tenascin C (TNC) (9), and fibronectin (FN) (10). In order to assess the role of particular matrix components on cellular responses, matrix spot arrays have been developed to screen for the relative effects of different ECM combinations on stem cell differentiation (11, 12), stellate cells during liver fibrosis (13), and niche formation by metastatic cancer cells (14). Such an array format provides equal opportunity for the cells seeded to land preferentially on any spot, effectively negating the bias that can occur in a multiwell format, while providing a high-throughput platform for screening applications (14, 15).

Further to the diversity of the ECM, the architecture and mechanical properties of the tissue are increasingly recognized as essential for function (16). In the body, the ECM composition and rigidity are highly variable between tissues, ranging from >1 MPa for bone and cartilage, to 10 to 100 kPa for skin and lung tissues, down to 0.1 to 10 kPa for brain and adipose tissue (16). Notably, during fibrosis or cancer progression, the normal deposition and density of matrix components is disrupted, leading to a stiffer microenvironment and a corresponding loss in tissue functionality, strongly correlating with the likelihood and severity of disease (5, 17–21). While many models include an ECM composition equivalent to that of the normal or disease state, few overlay this information

Author contributions: J.R.W.C., A.I., J.K.R., and J.I. designed research; J.R.W.C., A.I., G.F., V.H., E.J.-O., and E.P.O.V. performed research; N.P. and J.K.R. contributed new reagents/analytic tools; J.R.W.C., A.I., G.F., and E.J.-O. analyzed data; A.I. and G.F. edited the paper; and J.R.W.C. and J.I. wrote the paper.

The authors declare no competing interest.

This article is a PNAS Direct Submission.

[1]To whom correspondence may be addressed. Email: jdconw@utu.fi or joivaska@utu.fi.

This article contains supporting information online at https://www.pnas.org/lookup/suppl/doi:10.1073/pnas.2304288120/-/DCSupplemental.

Published October 16, 2023.

with a corresponding mechanical state representative of the modeled tissue, typically applying tissue culture plastics with a stiffness higher than that of bone. Thus, to address the mechanochemical signaling outcomes triggered by distinct ECM composition and matrix rigidity, we developed a high-throughput ECM printing approach on soft (0.5 kPa) and stiff (50 kPa) polyacrylamide hydrogels and monitored cell behavior in response to different matrix compositions and defined stiffnesses. Using this approach, we identified ECM compositions that uncouple cell spreading from matrix rigidity and support spreading on a soft substrate. Through computational modeling and experimental validation, we link this to an increase in cell-matrix connections and adhesion signaling on specific ECMs. Thus, we demonstrate contexts in which specific ECM compositions can dictate cellular mechanoresponses and dissociate the widely studied linear relationship of cell spreading and force with increasing substrate stiffness.

Results

Preferential Spreading of Different Cell Types on ECM Components at Defined Stiffnesses. Given the increasing evidence for the role of substrate stiffness in cellular responses, we printed a composite ECM protein microarray onto polyacrylamide gels of different stiffnesses (*SI Appendix*, Fig. S1*A*). These arrays were composed of seven ECM components [i.e., collagen I (ColI), Lam, ColVI, TNC, FN, hyaluronic acid (HA), vitronectin (VTN)], and poly-D-lysine (PDL), a substrate that supports cell adhesion and spreading via electrostatic interactions, either printed alone or in a 1:1 ratio with one of the other eight components (*SI Appendix*, Fig. S1*B*). The different components were found to adhere to both soft (0.5 kPa) and stiff (50 kPa) composite arrays, at titratable concentrations, with no visible cratering after ECM printing on either substrate (*SI Appendix*, Fig. S1 *C–F*).

Initial experiments with telomerase immortalized fibroblast (TIF; Fig. 1*A*) and U2OS osteosarcoma cells (Fig. 1*B*) seeded on soft and stiff arrays led us to the observation that cells on ECM mixtures spread better on soft substrates than those on a single ECM ligand (Fig. 1 *A* and *B*). To explore this further, we seeded TIF, MDA-MB-231 (MM231, breast cancer), and U2OS cells on soft and stiff composite ECM arrays (*SI Appendix*, Fig. S2). Furthermore, to assess the signaling in response to the different ECM ligands, we engineered cell lines to stably express a reporter for ERK activity (22), a key component of adhesion signaling cascades (1, 23, 24). Upon phosphorylation, the kinase-translocation reporter (KTR) applied herein is transported out of the nucleus, allowing monitoring of kinase activity within intact cells (*SI Appendix*, validation of KTR sensitivity to mitogen-activated protein kinase kinase (MEK)/ERK inhibitor in live cells shown in Movie S1 and *SI Appendix*, Fig. S3*A*, quantified in *SI Appendix*, Fig. S3*B*).

Altogether, we assessed 10 distinct cellular parameters on the soft and stiff ECM arrays: cell density, KTR ratio (nuclear vs. cytoplasmic); nuclear area and roundness (based on nuclear labeling); cell area and roundness (based on actin cytoskeleton labeling); integrin adhesion complex (IAC) number, area, shape (Feret) and size [detected as paxillin foci between 0.1 and 15 μm^2; *SI Appendix*, Fig. S4 (TIFs), *SI Appendix*, Fig. S5 (U2OS) and *SI Appendix*, Fig. S6 (MM231s)]. These parameters were then used as active variables for a principal component analysis (PCA) that was applied to plot the mean of each parameter on soft and stiff spots for each cell line and ECM mixture, finding that 62.1% of the variance was explained by the first two principal components (Fig. 1*C*). These allowed us to plot the relative contributions of each parameter to their respective components (Fig. 1*D*). From these data, we observed that cell size opposed the nuclear and cell shape (i.e., roundness) parameters, indicating that spread cells also tended to be more asymmetric, and that IAC count was less connected with IAC size, Feret and area than the three parameters were with one another. Interestingly, the variables of cell density and KTR ratio were poorly represented by these principal components, suggesting that they were less powerful for explaining the differences between conditions than the other parameters. When plotting the PCA, we observed higher cos2 values further from the center of the plot (Fig. 1*E*), indicating that those spots were better represented. In addition, the distribution of spots allowed effective visual separation of the different cell lines (Fig. 1*F*) and substrate stiffnesses (Fig. 1*G*). Notably, the MM231 cells remained largely unaffected by different ECM mixtures on a soft substrate, consistently displaying poor cell spreading, few adhesions, and a rounded morphology [Fig. 1*G*, MM231 cells on soft (0.5 kPa) are highlighted with a circle]. In contrast, on several ECM mixtures on a soft substrate, TIF and U2OS cells showed a "stiff-like" set of parameters (Fig. 1*G*, stiff-like spots labeled with their respective details), indicating that for these cell types, specific ECM compositions are supportive of a stiff-like phenotype on soft substrates.

Spreading on ColI/Lam and Lam/TNC Is Uncoupled from YAP (Yes-Associated Protein) Nuclear Translocation. To further explore the effects of the matrix compositions supporting stiff-like phenotypes, we next seeded TIFs on these ECM mixtures (Fig. 2). In accordance with the ECM array data, the mixtures of ColI/Lam and Lam/TNC supported cell spreading equally well on soft and stiff hydrogels (Fig. 2*A*, quantified in Fig. 2*B*). This was consistent in the U2OS cells for the ColI/Lam, but not the Lam/TNC mixture (*SI Appendix*, Fig. S7*A*, quantified in *SI Appendix*, Fig. S7*B*). In contrast, all of the individual ECM molecules, and many of the ECM combinations, showed the expected significant increase in cell spreading on the stiffer hydrogels compared to the soft [Fig. 2 *A* and *B*, compare soft (blue) and stiff (red)], indicating that the ECM mixtures of ColI/Lam, and in some cell lines Lam/TNC, have a specific ability to support stiff-like spreading of cells on soft matrices.

The transcriptional coactivator YAP is a key mechanotransducer that regulates proliferation and cell fate, and its nuclear translocation is supported by higher substrate rigidities, as well as cell spreading and stress fiber formation (25–27). Hence, to assess the molecular mechanoresponses associated with the different ECM compositions, we evaluated the nuclear localization of YAP on soft and stiff hydrogels (Fig. 2*C*, quantified in Fig. 2*D*; *SI Appendix*, Fig. S7*C*, quantified in *SI Appendix*, Fig. S7*D*). As expected, the levels of nuclear YAP were significantly higher on stiff than on soft substrates, consistent with the role of YAP in sensing the increased stiffness of the substrate. However, the increased spreading of cells on the mixtures ColI/Lam and Lam/TNC did not trigger an increase in YAP nuclear localization, suggesting that spreading alone is not sufficient to induce nuclear translocation in these cells on soft. This could be linked to the lack of obvious stress fibers on soft ColI/Lam and Lam/TNC and the reported ability of focal complexes to exert sufficient force to maintain a lamella and support cell spreading, even before maturation into a larger focal adhesion (FA) (28). Indeed, YAP nuclear translocation has been reported to require adhesion reinforcement, FA maturation, and sufficient formation of stress fibers (29, 30). Interestingly, two-dimensional nuclear cross-sectional area corresponded closely to cell area but not YAP nuclear localization, contrary to previous reports (29), implying a more nuanced relationship between cell spreading, nuclear stress and strain, and YAP activation on the different ECM mixtures (Fig. 2*C*, quantified in Fig. 2*E*; *SI Appendix*, Fig. S7*C*, quantified in *SI Appendix*, Fig. S7*E*).

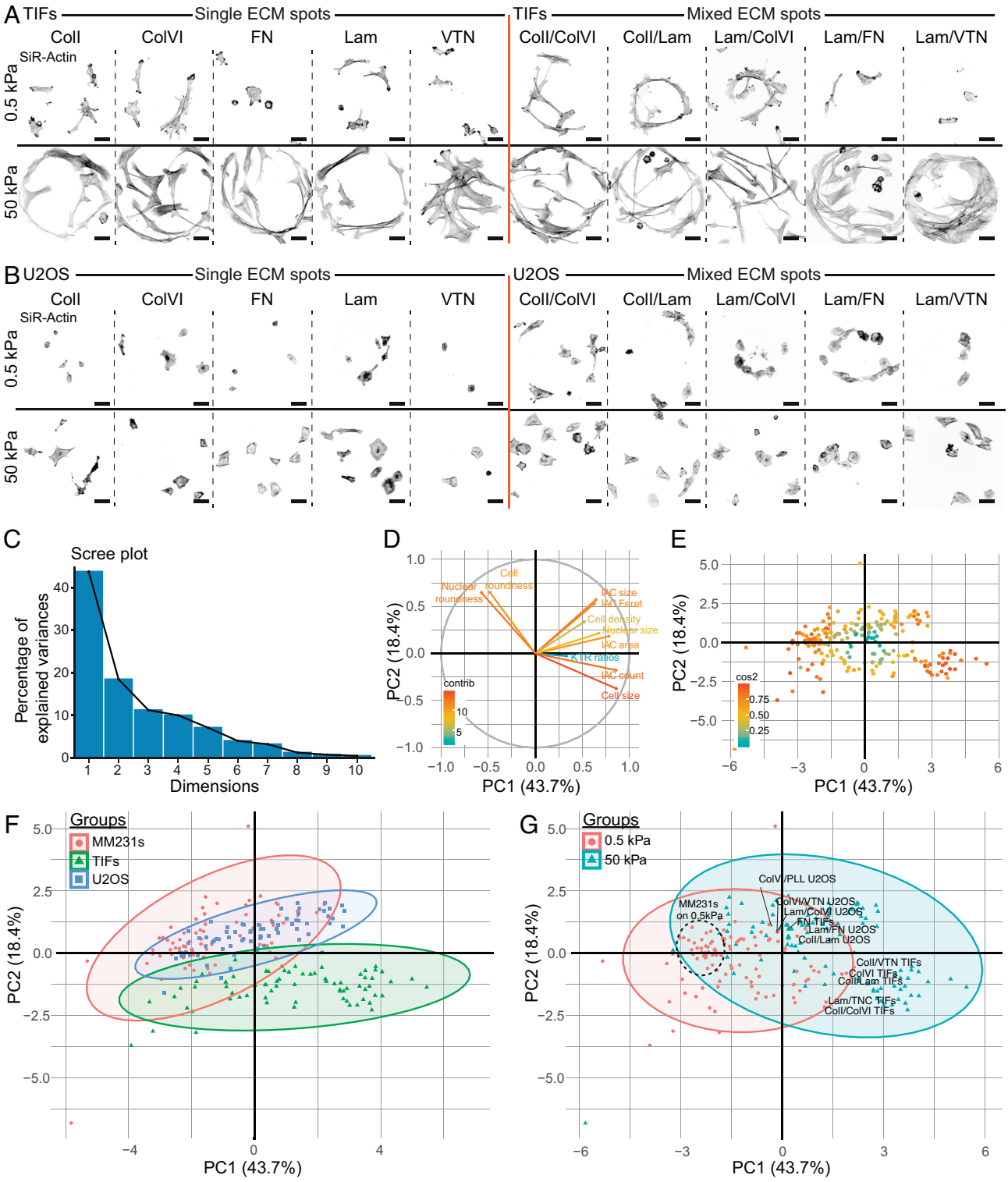

Fig. 1. ECM spot arrays on soft versus stiff hydrogels. (*A* and *B*) Representative images from TIF (*A*) and U2OS (*B*) cells seeded on 0.5 kPa or 50 kPa stiffness hydrogels with different ECM spots [n = 3 biological replicates, 4 spots/replicate/ECM mixture/stiffness; (Scale bar, 50 μm)]. (*C* and *D*) Scree plot of eigenvalues (*C*) and weighting the different parameters (*D*) from the PCA. (*E*) Factor map indicating the quality of representation by the principal components, where a high cos2 indicates a high degree of representation within the variable range from the PCA. (*F* and *G*) PCA using the median from each parameter on each ECM spot for both stiff and soft substrates (n = 3 biological replicates, 4 spots/replicate/ECM mixture/stiffness). Data are highlighted according to the cell line (*F*) or the substrate stiffness (*G*), where supportive mixtures on soft substrates are labeled. The complete ECM array datasets are included in *SI Appendix*, Figs. S4–S6).

Cells employ small GTPases to regulate their cytoskeleton, with the coordination of Rac1 and RhoA GTP-bound activities governing protrusion and retraction initiation and reinforcement (31–33). This careful balance in activity is essential for efficient cell migration and spreading (34, 35) and is often regulated by integrin-mediated signaling (36). This prompted us to explore whether changes in RhoA activity were associated with the increased cell spreading on supportive ECM mixtures on soft substrates. To this end, we employed a Förster resonance energy transfer (FRET) reporter [RhoA-2G, (37)], and fluorescence lifetime

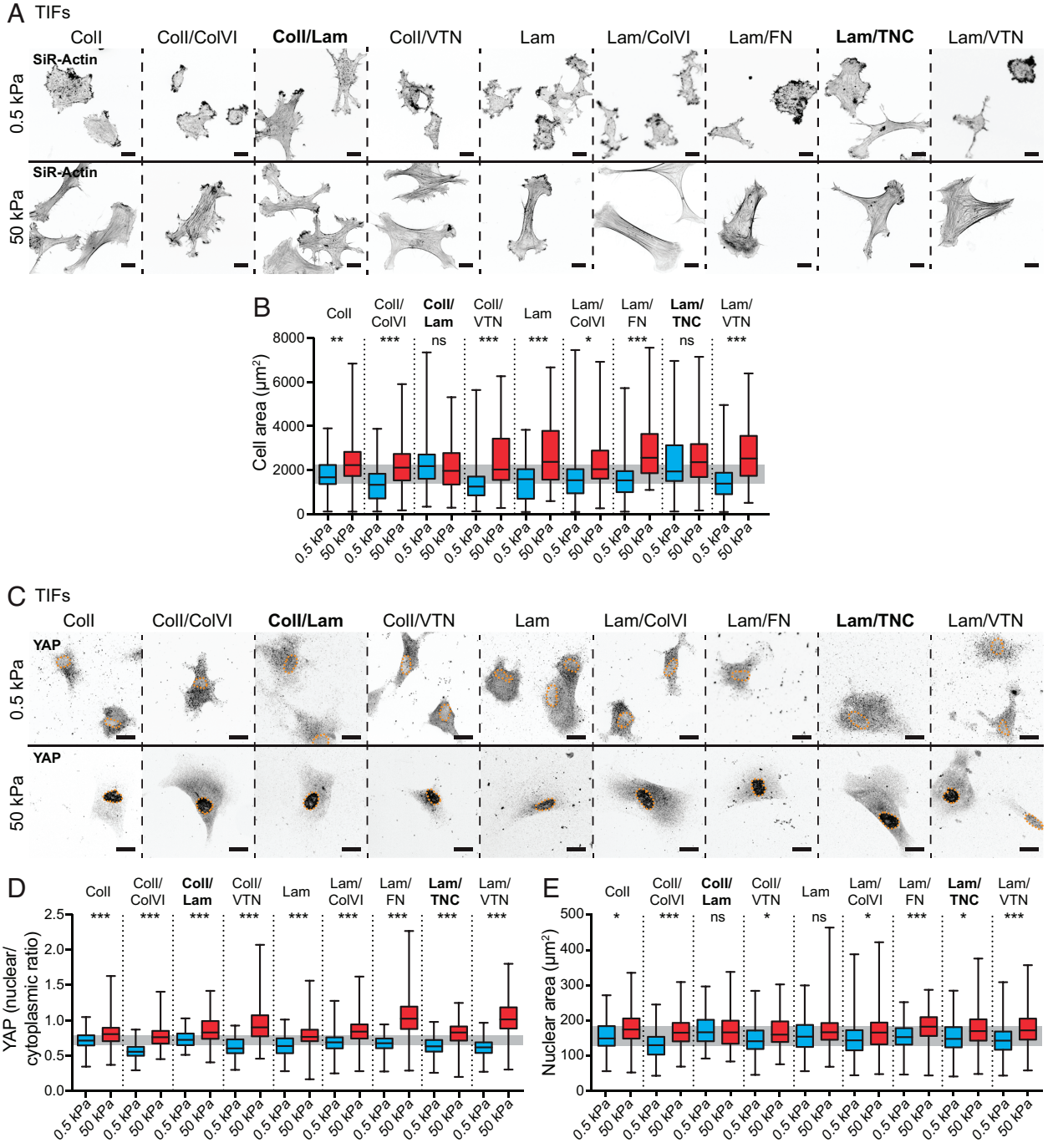

Fig. 2. Validation of ECM mixtures that support cell spreading on soft substrates. (*A* and *B*) Representative images (*A*) and quantification of cell area (*B*) after TIFs were seeded for 2 h on soft (0.5 kPa) and stiff (50 kPa) gels coated with different ECM mixtures, as indicated [n = 3 biological replicates, 13 to 59 cells/condition/replicate; (Scale bars, 20 μm); *P*-values from a one-way ANOVA with a Šidák correction for multiple comparisons; **P* < 0.05, ***P* < 0.01, ****P* < 0.001, and ns—not significant]. (*C*–*E*) Representative images (*C*) and quantification of YAP nuclear/cytoplasmic staining (*D*) and nuclear area (*E*) of TIFs seeded for 2 h on soft (0.5 kPa) and stiff (50 kPa) gels coated with different ECM mixtures, as indicated [n = 3 biological replicates, 13 to 59 cells/condition/replicate; (Scale bars, 20 μm); *P*-values from a one-way ANOVA with a Šidák correction for multiple comparisons; **P* < 0.05, ***P* < 0.01, ****P* < 0.001, ns—not significant]. Gray bars are drawn to mark the interquartile range of the control ColI 0.5 kPa condition in boxplots. Nuclei are marked with orange dashed lines (*A* and *C*).

imaging microscopy (FLIM)-FRET to read out relative changes in RhoA activation state in U2OS cells (*SI Appendix*, Fig. S8*A*). Concordant with previous reports for different cell types (36), all of the ECMs demonstrated an increased RhoA activation state on the stiffer 50 kPa substrates (*SI Appendix*, Fig. S8*B*, quantified in *SI Appendix*, Fig. S8*C*). While established RhoA activators, RhoA guanine nucleotide exchange factor, GEF-H1 (*SI Appendix*, Fig. S8*D*), and treatment with calpeptin increased RhoA activity (*SI Appendix*, Fig. S8*E*), we observed no consistent differences in RhoA activity between cells adhering to ColI/Lam mixture and the Lam and ColI alone on the softer 0.5 kPa gels (*SI Appendix*, Fig. S8 *B* and *C*). Together, these results suggest that altered balance in small GTPase activity is not likely to explain the increased spreading on ColI/Lam on the soft substrates.

Increased Clutch Numbers Can Explain the Increased Spreading of Cells on Soft ECM Mixtures. In order to test the role of integrins in the increased spreading of cells on specific ECM mixtures on soft, we treated TIFs on ColI/Lam with integrin β1 function-blocking antibodies (AIIB2 and mAb13), which block integrin-mediated

adhesion to ColI and Lam (Fig. 3*A*, quantified in Fig. 3 *B* and *C*). These antibodies severely compromised cell spreading on stiff and soft substrates, indicating a key role for integrins in the increased spreading on ColI/Lam and Lam/TNC on soft. These data also suggest that while mature FAs might be absent on soft substrates, the formation of IACs remains an important factor for cellular function. To further characterize TIF IACs on different ECM compositions, we investigated their subcellular distribution, comparing cells on single ECMs and the ColI/Lam mixture. The centripetal movement of IACs is often linked to their maturation from nascent to FAs, and can be indicative of cytoskeletal forces being exerted on these complexes. However, we observed minimal differences in IAC localization in TIFs seeded on ColI, Lam or the mixture of ColI/Lam (*SI Appendix*, Fig. S9). Next, in order to study the compositional heterogeneity of these IACs, we stained for zyxin and vinculin (*SI Appendix*, Fig. S10 *A* and *B*). Zyxin is an adhesion component with a particularly fast turnover (38, 39). Like vinculin, zyxin's recruitment to IACs has been linked

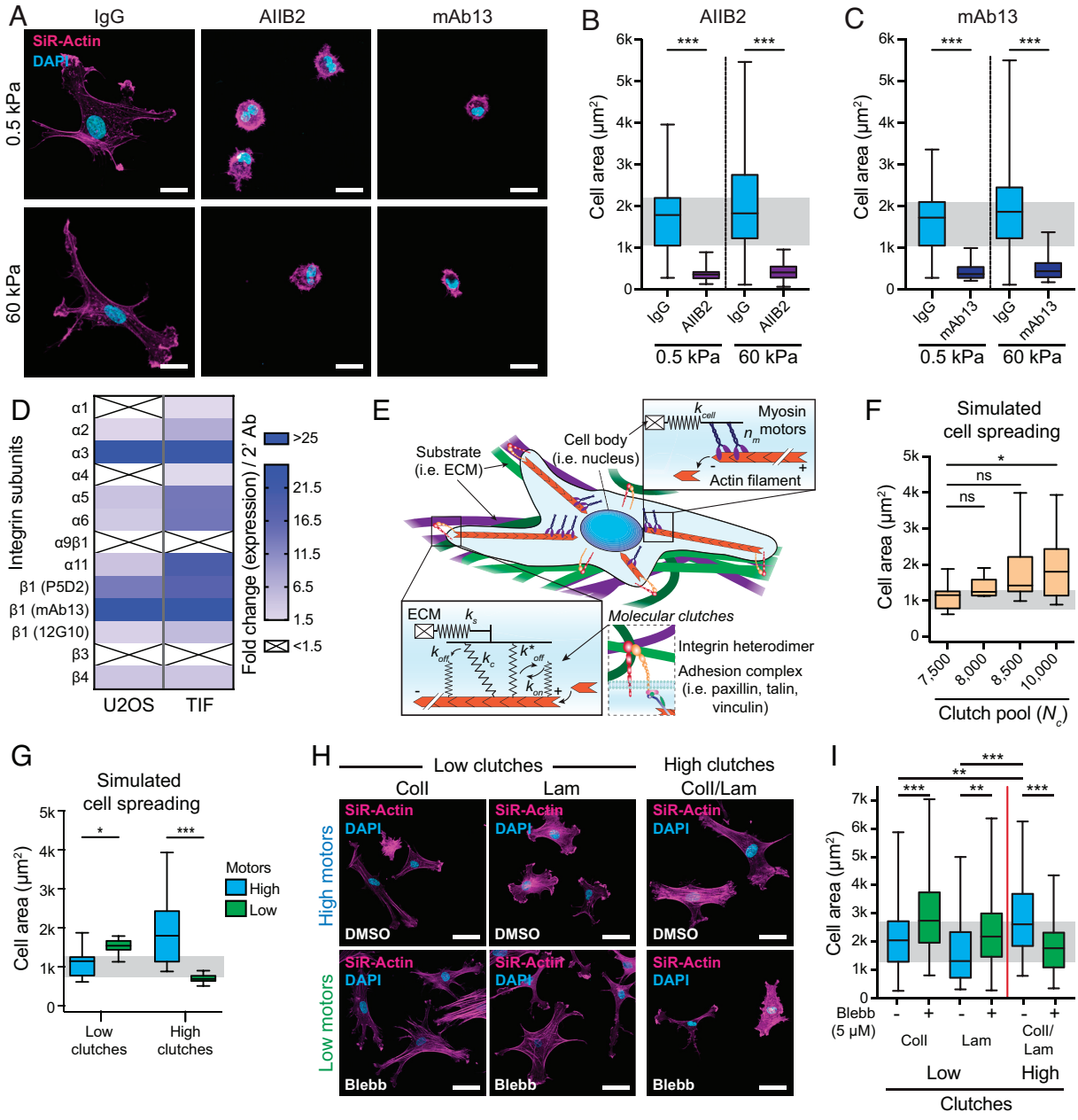

Fig. 3. Improved cell spreading on soft substrates can be explained by an increase in the number of molecular clutches. (*A*–*C*) Representative images (*A*) and quantification (*B* and *C*) of TIFs seeded for 2 h on 0.5 or 60 kPa hydrogels coated with ColI/Lam, treated with AIIB2 (*B*, 10 μg/mL) or mAb13 [*C*, 10 μg/mL; (Scale bars, 20 μm); n = 3 biological replicates, 12 to 25 cells/condition/replicate; *P*-values from a one-way ANOVA with a Tukey correction for multiple comparisons; ***$P < 0.001$]. (*D*) Flow cytometry to assess the relative surface expression of different integrin isoforms and heterodimers on TIF and U2OS cells (n = 5 biological replicates). (*E*) Schematic of the motor-clutch model used to simulate spreading of cells with different numbers of molecular clutches or motors. See *Methods* and *SI Appendix*, Table S1 for more details. (*F*) Simulation of cell spreading with an increasing number of available clutches (N_c) on a soft substrate (k_s = 0.5 pN/nm). The gray band indicates the interquartile range from the control (N_c = 7,500) condition (n = 6 to 12 simulated cells/condition; Kruskal–Wallis test with a Dunn's correction for multiple comparisons; *$P < 0.05$). (*G*) Simulation of cell spreading on a soft substrate with high or low number of clutches and motors (k_s = 0.5 pN/nm; high N_c/N_m ~ 10,000; low N_c/N_m ~ 7,500; 9 to 12 simulations/condition; *P*-values from a Kruskal–Wallis test with a Dunn's correction for multiple comparisons; *$P < 0.05$, ***$P < 0.001$). The gray band indicates the interquartile range from the control (low clutches/high motors) condition. (*H* and *I*) Representative images (*H*) and quantification (*I*) of TIFs seeded for 2 h on 0.5 kPa hydrogels coated with ColI, Lam, or ColI/Lam, treated with Blebbistatin (Blebb; 5 μM) or DMSO control. [(Scale bars, 50 μm); n = 3 biological replicates, 16 to 41 cells/condition/replicate; *P*-values from a one-way ANOVA with a Tukey correction; **$P < 0.01$ and ***$P < 0.001$].

to external and internal forces and is supported by vinculin tension, irrespective of adhesion maturation or stress fiber linkage (40–43). The number of zyxin- and vinculin-positive foci correlated with cell spreading in the different conditions with more zyxin and vinculin-positive foci detected in cells spreading on the ECM mixture on soft, suggesting improved cell-matrix interaction on soft substrates coated with ColI/Lam mixture compared to the single ECMs (*SI Appendix*, Fig. S10 *C–E*). Taken together, these results suggest that TIFs on soft ColI/Lam substrates present with more IACs than cells on ColI or Lam alone, but do not support the idea that this would correlate with increased IAC maturation, or the forces exerted on individual adhesions.

As the integrin β1 subunit is shared by the majority of ECM-binding integrins, we assessed the surface expression of different integrin heterodimers on TIF and U2OS cells (Fig. 3*D* and *SI Appendix*, Fig. S11). Both cell types expressed the main ColI-binding integrins, α2β1 and α11β1, as well as the primary Lam-binding integrins α3β1, α6β1, and α6β4, demonstrating that on a ColI/Lam mixture these cells are able to employ a broader repertoire of adhesion receptors than on either matrix alone.

This, together with the increased number of IACs on soft ColI/Lam substrates, prompted us to hypothesize that increased ligand diversity was resulting in increased integrin engagement, by the virtue of a larger number of potential cell-ECM binding sites being available to the cell. To investigate the effects of an increased propensity for integrin-ECM engagement on a soft substrate with a mixed ECM, we employed a motor-clutch model developed to explain stiffness-dependent cell migration, and more recently durotaxis (44–46). The model describes a ligand-binding unit (clutch) composed of an adhesion receptor (i.e., an integrin heterodimer) and the adaptors linking it to the actin cytoskeleton (Fig. 3*E*, the clutch assembly is represented in the model by a single bond). The "motor" unit represents the actomyosin contractile force that is transmitted to the substrate through clutches to enable cell spreading and motility [for more details on the model, see *SI Appendix, Extended Methods* and (45–48)]. Previous work has shown that altering the ratio of clutches to motors, that is, the amount of cell adhesion molecules relative to intracellular contractility, can drastically affect cell behavior, including the capacity to exert traction or migrate on a given substrate stiffness (46, 47). Using this model, we altered the total number of molecular clutches (N_c; i.e., potential integrin-ECM connections, available to each cell), while maintaining substrate rigidity (spring constant) at 0.5 pN/nm to mimic our soft hydrogels (*SI Appendix*, Table S1). Through these simulations, we found that an incremental increase in the number of clutches, relative to motors, results in a steady increase in the average cell area, indicative of cell spreading on a soft substrate (Fig. 3*F* and Movie S2). We next simulated the outcome of tuning cell contractility (increasing or decreasing motor number) relative to the clutch number. These simulations predicted that in cells with a low clutch number, a decreased motor number increases cell area; whereas in cells with a higher number of clutches, lowering the motor number decreases cell spreading (Fig. 3*G*). To test these predictions, we then treated TIFs plated on ColI, Lam or ColI/Lam mixture with low doses of the myosin II inhibitor Blebbistatin. In concordance with the model, decreasing motor number using Blebbistatin increased cell spreading on single ECM molecules by ≥50% and reverted the stiff-like increased cell spreading on soft ColI/Lam to a similar degree as that observed with DMSO-treated cells on single ECMs (Fig. 3*H*, quantified in Fig. 3*I*). These data further suggest that cell spreading on soft is a delicate balance between cell adhesion and cell contraction dynamics and is favored by a slightly higher clutch:motor ratio; a scenario potentially supported by a more complex ECM environment. However, the synergistic effect on cell spreading on soft was not observed with all ECM combinations (Figs. 1 and 2), indicating that the repertoire of integrins engaged and downstream signaling to the cytoskeleton are also essential in determining the outcome of cell adhesion to complex ECM mixtures as a function of substrate rigidity.

Increased Spreading on Soft Substrates with Mixed ECMs Corresponds with a Concomitant Increase in Adhesion Signaling. To assess the biological outcome of increased cell spreading on specific ECM mixtures, we returned to the ECM array ERK activation data (ERK KTR signal; Fig. 4*A* and *SI Appendix*, Fig. S4*B*). Notably, there was a significant increase in ERK activation in TIFs on ColI/Lam, compared to ColI or Lam alone on soft substrates (Fig. 4*B*, quantified in Fig. 4*C*). As the MAPK pathway is activated by IACs (2, 23, 24), we then revisited the simulations and investigated the relationship between the available pool of clutches and the number of clutches engaged by the ECM at any given time. The motor-clutch computational modeling predicts that increasing the pool of available clutches by 25% significantly increases mean clutch engagement in cells on a soft substrate (Fig. 4*D*). To investigate this experimentally, we assessed the activation state of integrins on single and mixed ECMs on a soft substrate. As active, ligand-engaged integrin β1 adopts an extended-open conformation (2, 49), we applied an antibody specific to ligand-engaged integrin β1 [12G10; (50)] to assess the relative integrin β1—ECM engagement between conditions. In concordance with the predictions of the model, we observed lower levels of active integrin β1 heterodimers in the soft Lam and ColI conditions, compared to the significantly higher integrin activity on the ColI/Lam mixed ECM on soft substrates (Fig. 4*E*, quantified in Fig. 4*F*). In line with the increased ERK activity observed with the KTR (Fig. 4 *B* and *C*), and the increased level of active integrin β1, phosphorylated FA kinase (pFAK) was also significantly higher on the mixed ECM (Fig. 4*E*, quantified in Fig. 4*G*). On collagen, where adhesion is mediated by α1β1, α2β1, and α11β1 (Fig. 3), activated integrin β1 and pFAK showed a high degree of colocalization (*SI Appendix*, Fig. S12), as expected. Interestingly, this colocalization between the active integrin β1 and pFAK signals was lower on Lam than ColI and intermediate on the ColI/Lam mixture. This suggests that in ECM conditions with Lam present, the Lam-specific α6β4 integrin, not recognized by 12G10, may be synergizing with the Lam-binding α3β1 and α6β1 integrins in mediating adhesion and downstream signaling to FAK (*SI Appendix*, Fig. S12). Activation of FAK through autophosphorylation is one of the first steps in integrin signaling and occurs already in nascent adhesions, in addition to mature FAs (2, 38). Therefore, the supportive ECM mixture on soft not only facilitates stiff-like spreading but also triggers key integrin-proximal signaling pathways on soft matrices by engaging multiple integrin subtypes. Cumulatively, we see that the mixed ECMs can provide an efficient signaling response, as cells are able to apply a larger number of integrin receptors to interact effectively with softer substrates (Fig. 4*H*). This supports the observation that specialized cell types in multicellular organisms can function effectively in very soft environments and provides a springboard for future work into the diversity of ECM combinations, organizations, and modifications that permit such multifaceted cellular activities.

Discussion

Here, we have developed a composite ECM spot array system that combines the assessment of cellular responses with that of matrix composition and the mechanical properties of the adhered

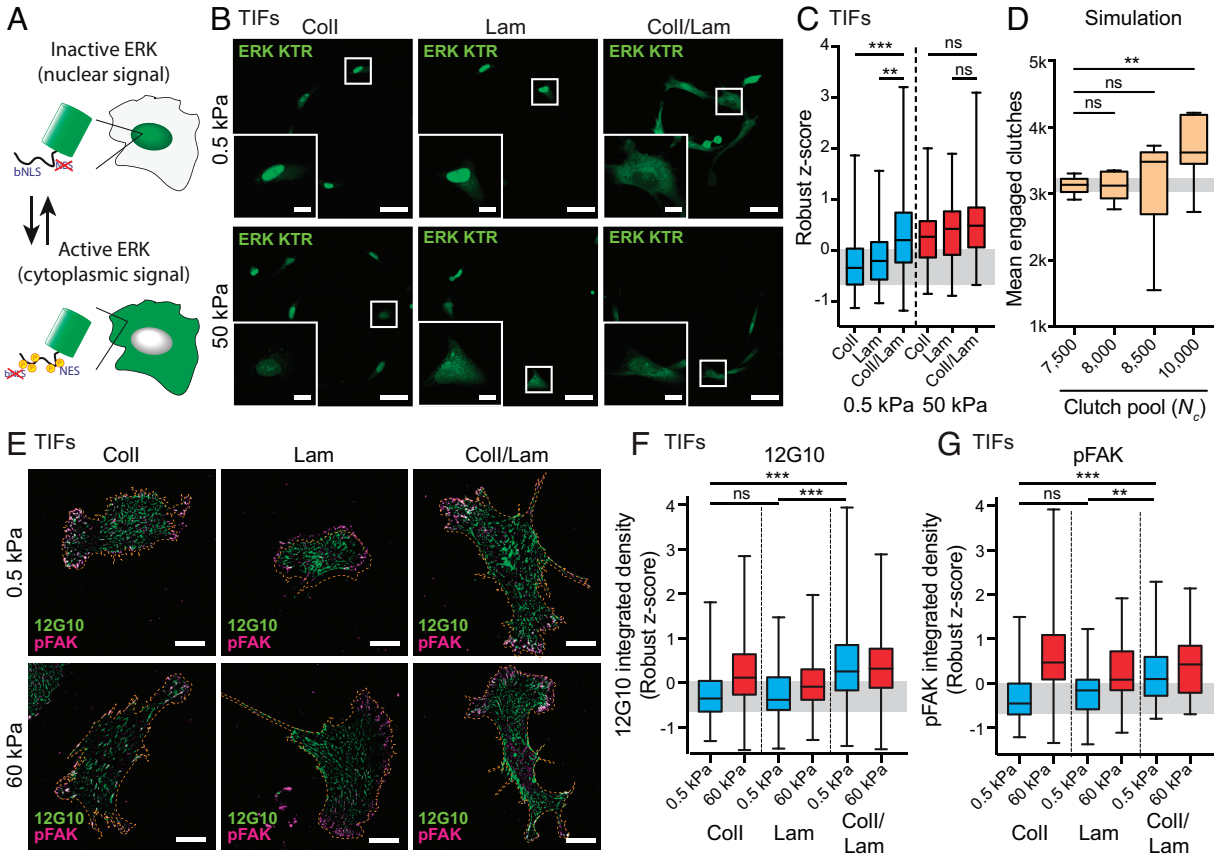

Fig. 4. Increased spreading occurs in conjunction with a concomitant increase in integrin signaling. (*A*) Schematic of the ERK KTR activity reporter, where high ERK activity leads to an increase in phosphorylation and inactivation of the bNLS and shuttling out of the nucleus. (*B* and *C*) Representative images (*B*) and quantification (*C*) of the ERK KTR reporter expressed in TIF cells seeded on ECM array spots [scale bars, 50 μm (main), 10 μm (*Insets*); n = 3 biological replicates, 4 spots/ECM mixture/substrate/replicate; *P*-values from a one-way ANOVA with a Šidák correction for multiple comparisons; $^{**}P < 0.01$, $^{***}P < 0.001$, and ns—not significant]. (*D*) Mean number of engaged clutches in simulated cells with an increasing number of total available clutches (N_c), on a soft substrate (k_s = 0.5 pN/nm). The gray band indicates the interquartile range from the control (7,500 N_c) condition (n = 6 to 12 simulated cells/condition; Kruskal–Wallis test with a Dunn's correction for multiple comparisons; $^{**}P < 0.01$). (*E–G*) Representative images (*E*) and quantification (*F* and *G*) of TIFs seeded for 2 h on 0.5 or 60 kPa stiffness gels coated with Coll, Lam or Coll/Lam and stained for 12G10 (*F*, n = 5 biological replicates) and pFAK [*G*, n = 3 biological replicates; 12 to 25 cells/condition/replicate; (Scale bars, 20 μm); *P*-values from a one-way ANOVA with a Tukey correction for multiple comparisons; $^{*}P < 0.05$, $^{***}P < 0.001$, and ns—not significant]. Gray bars are drawn to mark the interquartile range of the control Coll 0.5 kPa condition in boxplots (*C*, *F*, and *G*).

substrate. Through this screening platform, we uncovered ECM compositions that uncouple cell spreading from stiffness and promote stiff-like cell behavior on more compliant substrates. This unexpected in vitro observation is in line with the fact that cells in soft tissues are similarly capable of functioning without a rigid support. In line with this finding, we applied a computational motor-clutch model to simulate cell spreading on soft substrates as a function of ECM ligand availability and demonstrated that a higher number of molecular clutches (i.e., available integrin-ECM bonds) could compensate for the lack of mechanical support provided by the substrate, effectively promoting spreading. We then verified experimentally the fundamental predictions of the model: that cell spreading on soft ECM depends on the balance between available clutches and motor activity, and that the number of functional integrin-ECM bonds scales with the overall availability of integrin-ECM binding sites. Collectively, the high-throughput screening, modeling, and experimental validation uncover a mechanosensing paradigm, where cell spreading and integrin downstream signaling are equivalently activated on soft and stiff substrates under specific matrix conditions.

Several studies have looked at the force-mediated activation of integrins, where affinity is increased with loading, giving rise to talin unfolding and vinculin recruitment, which enables adhesion reinforcement by preventing talin refolding and subsequently facilitating adhesion maturation (40, 41). On soft substrates, however, mechanical adhesion reinforcement is less likely to occur, which has led to the notion that cells have a compromised ability to transmit ECM-induced signals (48). This suggests that factors such as ligand density and the varied affinities of integrins to different ligands may play a larger role in effective cell adhesion on softer substrates (49). To exemplify the varied application of integrin heterodimers, cells adhering to FN commonly apply integrin β3 heterodimers for the formation of small nascent adhesions, while larger adhesions are stabilized with integrin β1 heterodimers (51). Similarly, the affinity of different integrin β1 heterodimers has been linked to conformational changes that radically modulate the on and off rates for ligand binding (52). Furthermore, the expression of different collagen-binding integrins, with distinct binding affinities to fibrillar or nonfibrillar collagens (53–55), or to defined Lam subtypes (56), highlights the varied application of integrin heterodimers even within the same ligand-binding family. These studies, and the data presented herein, place a spotlight on the biological complexity of cell-ECM interactions, extending beyond the role of any factor in isolation. They are also likely to explain why only some of the ECM mixtures present in our compliant substrate arrays supported stiff-like phenotypic changes, while others did not.

A shift in drug discovery strategies away from target-based approaches and toward image-based phenotypic screening highlights the challenge of efficacious targeting of disease states and

the power of modern microscopy to overcome such challenges (57). Recent studies assessing the efficacy of treatment responses between 2D plastic and 3D systems in ECM gels have helped to explain the high attrition rates of compounds in clinical trials, where the mechanical and compositional properties of the ECM in vivo have a significant effect on drug efficacy at later stages of the drug discovery pipeline (58). This is particularly evident in relation to cancer therapy, where solid tumors with a higher stiffness show increased radio- and chemoresistance (17, 59), which changes upon therapeutic intervention to a softer matrix and altered responses to therapies (60, 61). In line with the importance of the ECM, the progression of several cancer subtypes can be more robustly predicted using gene signatures from the stromal compartment, than from the cancer cells themselves (62–65). The convoluted relationship between the tumor and associated stroma/ECM is further illustrated by the suppressive role of healthy stroma on cancer cell growth (4), while the cancer-associated stroma is linked to both disease containment and prosurvival niche formation (66). Our data, and the many studies showing distinct cell behaviors on substrates of differing stiffnesses, imply that screening platforms encompassing matrix rigidities and ECM compositions tailored to align with the in vivo situation of the given tumor type would be expected to be significantly more relevant.

Here, we present a platform for assessing matrix composition in the context of different rigidities to screen for mixtures supportive of spreading and intracellular signaling responses. Aligning computational modeling and experimental validation, we uncovered 'stiff-like' cell spreading and signaling on soft matrices as being dependent on increased engagement of a more diverse range of integrin heterodimers on a mixed matrix. Thus, this work demonstrates the importance of considering the vast array of ECM combinations, modifications, stiffnesses, as well as the interacting cell types, that occur in tissues and are essential to our understanding of both healthy and disease states.

Methods

Polyacrylamide Hydrogels with Defined Stiffnesses. Commercial [Softview Easy Coat hydrogels, 35 mm dish with 10 mm glass bottom, SV3510-EC-0.5-EA (0.5 kPa) or SV3510-EC-50-EA (50 kPa)] or in-house stiffness gels were used as indicated. In-house gels were prepared using glass-bottom dishes (D35-14-1N, Cellvis). The dishes were treated with bind silane solution [71.4 μL Bind Silane ([3-(Methacryloyloxy)propyl]trimethoxysilane; Sigma, M6514), Glacial Acetic Acid (71.4 μL; Sigma, 33209) up to 1 mL in Ethanol (96%)] for 30 min at room temperature and then wash twice with ethanol (96%). 12 μL of gel mixture [0.5 kPa: 63 μL 40% Acrylamide Solution (Sigma, A4058), 10 μL 2% bis-acrylamide solution (Sigma, M1533), 399 μL PBS, 2.5 μL 20% ammonium persulfate (APS; Sigma, A3678, diluted in Milli-Q water) and 1 μL TEMED (Sigma, T9281); 60 kPa: 225 μL 40% Acrylamide Solution, 100 μL 2% bis-acrylamide solution, 175 μL PBS, 2.5 μL 20% APS and 1 μL TEMED] was applied to dry, bind silane treated dish(es) and overlaid gently by placing 13 mm glass coverslips on top of the gel mixture, allowing it to set for 1 h at room temperature, as described previously (67). A sufficient amount of PBS was then added to cover the coverslip completely before carefully removing the coverslip. Surface activation was performed with Sulfo-Sanpah (sulfosuccinimidyl 6-(4′-azido-2′-nitrophenylamino)hexanoate; 0.2 mg/mL in 50 mM HEPES; Thermo Fisher Scientific, 22589) and EDC (N-Ethyl-N′-(3-dimethylaminopropyl) carbodiimide hydrochloride; 2 mg/mL in 50 mM HEPES; Sigma, 03450), applied to the surface for 30 min at room temperature with gentle agitation. Gels were then incubated in a UV oven (UVO-cleaner 342 to 220, Jelight Company) at 5 cm distance for 10 min before washing thrice with PBS. Commercial or in-house hydrogel coating was performed with saturating concentrations of all ECM mixtures at 20 μg/mL final ECM concentration (*SI Appendix*, Fig. S13).

Cell Lines. Human dermal fibroblasts, TIFs [a kind gift from J.C. Norman (Beatson Institute, Glasgow, Scotland, UK)], MM231 (HTB-26, ATCC), HEK293FT (R70007, ThermoFisher), and U2OS (HTB-96, ATCC) cells were maintained in Dulbecco's modified Eagle's medium (Sigma, D5796) supplemented with 10% serum (FBS; Biowest, S181T), L-glutamine (100 mM, Sigma, G7513), HEPES (10 mM, Sigma, H0887), and sodium pyruvate (1 mM, Sigma, S8636).

Composite ECM Spot Arrays. ECM mixtures at 400 μg/mL were prepared in printing buffer (RPMI, 20 mM HEPES, 17 mM EDTA, 0.6 M sucrose) using PDL (A-0030E, Sigma), FN (Millipore, 341631), ColI (Millipore, 08 to 115), TNC (Merck, CC065), HA (HyStem Cell Culture Scaffold Kit, HYS010-1KT, Sigma-Aldrich), Lam EHS (Sigma-Aldrich, L2020), ColVI (Abcam, ab7538), and VTN-N (purified as in ref. 68). Arrays were printed on commercial stiffness gels (Softwell 24-well plate Easy coat, SW24-EC-0.5-EA, SW24-EC-50-EA, Matrigen) using an OmniGrid (Gene Machines) microarray printer with 200 μm solid tip pins (PTLS200, 401774, PointTechnologies). Printed arrays were then blocked with 1% bovine serum albumin (BSA; A8022, Sigma) in phosphate-buffered saline (PBS; Biowest, L0615) overnight at +4 °C. 2×10^5 TIF, MM231, and U2OS cells were blocked in 1% BSA and then seeded on 0.5 and 50 kPa spot arrays in 24-well wells for 2 h prior to fixation for 10 min at 37 °C in 4% PFA in PEM buffer [EGTA (10 mM; VWR Chemicals, 0732), $MgSO_4$ (1 mM; Fluka Analytical, 00627), PIPES (pH 6.9; 100 mM; Sigma, P6757), sucrose (75 mM; Sigma, S9378), and Triton X-100 (0.2%; Sigma, T8787) in H_2O].

Collagen Labeling. To fluorescently label rat tail type I collagen (~4.24 mg/mL, 354236, Corning), 1.65 mL was mixed with 450 μL of Milli-Q water and 500 μL of neutralizing buffer (20 mM NaH_2PO_4, 112 mM $Na_2HPO_4 \cdot 2H_2O$, 0.4 M NaCl, and 46 mM NaOH) and incubated at 37 °C for 30 min. The polymerized collagen was then washed thrice with PBS for 10 min. Then, 3 mL of Milli-Q water and 1 mL of bicarbonate buffer [1 M $NaHCO_3$ (pH 8), raised dropwise to pH 8.3 using 1.17 M Na_2CO_3 (pH 11)] were added to the collagen gel before addition of the Alexa Fluor™ 647 NHS Ester (Succinimidyl Ester) dye (A20006, Invitrogen) in 100 μL of PBS. After incubating the collagen mix overnight at 4 °C, the dye was then removed, and the collagen was washed with PBS with rotation at room temperature for 30 min, changing the PBS five times. Stained collagen was then depolymerized through the addition of 2 mL HCl (20 mM) and gentle rotation at 4 °C overnight. The collagen was finally centrifuged at 20,000 g for 10 min, collecting the labeled collagen from the supernatant.

Flow Cytometry of Surface Integrin Isoforms. Cells from 2D culture plates were trypsinized and then fixed with 2% PFA for 10 min at 37 °C before washing twice with PBS. A total of 200,000 cells were incubated with primary antibodies (1:100 dilution in Tyrode's buffer [ITGA1 (MAB1973, Millipore), ITGA2 (MCA2025, Bio-Rad), ITGA3 (ab228485, Abcam), ITGA4 (MAB16983, Millipore), ITGA5 (ab78614, Abcam), ITGA6 (MCA699, Serotec), ITGA11 (MAB4235, R&D Systems), α9β1 (sc-59969, Santa Cruz), ITGB3 (ab179473, Abcam), ITGB4 (ab29042, Abcam), active β1 (clone 12G10, in-house production from Developmental Studies Hybridoma Bank (DSHB) hybridoma), β1 (clone P5D2, in-house production from DSHB hybridoma), and inactive β1 (clone mAb13, in-house production from DSHB hybridoma)]) for 1 h at 4° C with gentle agitation before washing twice with PBS and incubating with secondary antibodies (Alexa-488 conjugated Anti-Mouse/Anti-Rat Invitrogen; 1:300 dilution in Tyrode's buffer) for a further hour at 4 °C with gentle agitation. Cells were then washed again with PBS before being resuspended in 200 μL of PBS and loading into a 96-well plate. Cytometry was then performed on an LSRFortessa cell analyzer using the High-Throughput Sampler (BD Biosciences). Up to 10,000 single-cell events were collected per condition. Gating and statistical analysis of the cell population were performed in FlowJo (BD Biosciences).

Frequency-Domain FLIM-FRET. All FLIM experiments were performed on a LIFA fast frequency-domain FLIM system (Lambert Instruments) attached to an inverted microscope (Zeiss AXIO Observer.D1) with sinusoidally modulated (40 MHz) epi-illumination (1 W) at 406 nm from a temperature-stabilized multi-LED system (Lambert Instruments) and a 63×/1.15 objective (Zeiss, Objective LD C-Apochromat 63×/1.15 W Corr M27). Atto425 (Sigma, 56759) in PBS at 1 μM, pH 7.4, was used as a lifetime reference standard. An appropriate filter set for mTFP1 was used (No excitation filter; beam splitter, FT 455; emission, BP 475/20) in order to measure per cell, the phase and modulation fluorescence lifetimes per pixel from images acquired at 12 phase settings, using the manufacturer's software. The apparent FRET efficiency (E_{app}) was calculated using the measured lifetimes of each donor–acceptor pair (τ_{DA}) and the average lifetime of the donor-only (τ_D) samples. For all experiments, the donor-only samples were parental U2OS cells that had been

transfected with pEF.DEST51-mTFP1(cp227) overnight using Lipofectamine 3000 (ThermoFisher, L3000015), as per the manufacturer's protocol.

$$E_{app} = (1 - \tau_{DA} / \tau_{D}) \times 100.$$

For the 30-min calpeptin (50 μM; Selleckchem, S7396) treatments, U2OS cells stably expressing the RhoA-2G FRET reporter were seeded overnight in glass-bottom 24-well wells (Cellvis, P24-1.5H-N) with DMSO as a control. Similarly, for the transfections with pEF.DEST51-mScarlet and pDEST-mCherry-ARHGEF2, U2OS cells stably expressing the RhoA-2G FRET reporter were seeded overnight in glass-bottom 24-well wells, transfecting after 6 h seeding using Lipofectamine 3000, as per the manufacturer's protocol. Experiments on stiffness gels were performed on 0.5 kPa or 50 kPa gels in 24-well wells after first coating with different ECM components and blocking with 2% BSA. These coated gels were then seeded with BSA-blocked RhoA-2G-expressing U2OS cells for 2 h at 37 °C. All experiments were fixed for 10 min at 37 °C in 4% PFA before washing with PBS and 1M glycine and imaging as above.

Immunofluorescence. Prior to seeding with TIF or U2OS cells, in-house (details above) or commercial stiffness gels were coated with ECM mixtures in PBS at 37 °C for 1 h and then blocked with sterile 2% BSA for a further hour at 37 °C. Cells were also blocked in 2% BSA before seeding for 2 h on coated gels, prior to fixation for 10 min at 37 °C in 4% PFA in PEM buffer. Treatment with Blebbistatin (5 μM; STEMCELL Technologies, 74202), or Integrin function-blocking antibodies against integrin β1 (clones mAb13 and AIIB2, in-house production using hybridomas from DSHB) or IgG [Rat IgGa, kappa monoclonal (RTK2758)–Isotype control; Abcam, ab18450] occurred during cell seeding where indicated. Fixed samples were then blocked in blocking buffer (2% BSA and Glycine (1 M; PanReac AppliChem, A1067) in PBS) overnight at 4 °C. Cell nuclei were stained with Hoechst 33342 (1:1,000, ThermoFisher, 62249), SiR-Actin (1 μM, Spirochrome, sc001) in parallel with primary antibodies against paxillin [(Y113); 1:100, Abcam, ab32084], zyxin (EPR4302; 1:100, Abcam, ab109316), vinculin (1:100, Sigma, V9131), active β1 (1:25 from 0.25 mg/mL stock (in-house production); clone 12G10), ColI (1:200, Abcam, ab34710), FN (1:100, Sigma, F3648), Lam (1:100, Sigma, L9393), p-FAK(Y397) (1:100, Cell Signaling, 8556), and/or YAP (63.7; 1:100, Santa Cruz, sc-101199) in PBS overnight at 4 °C. Samples were then washed twice with PBS before staining with appropriate secondary antibodies for 1 h at room temperature and a further two washes with PBS. Imaging was performed on a Zeiss 3i CSU-W1 spinning disk confocal microscope using SlideBook 6 acquisition software and a 40×/1.1 Zeiss LD C-Apochromat or 63×/0.75 Zeiss LD Plan-NEOFLUAR objectives with water immersion. Analysis of microscopy data was performed in Fiji (NIH), assessing colocalization using Pearson's coefficients from the Coloc2 plugin.

Lentiviral Transduction. Lentivirus transduction was used to generate cell lines (TIF, MM231, and U2OS) stably expressing the ERK KTR, or RhoA-"G FRET reporters. The lentiviruses were produced in HEK293FT cells by cotransfecting with a third-generation lentiviral packaging system composed of pMDLg/pRRE (Addgene plasmid #12251), pRSV-Rev (Addgene plasmid #12253), pMD2.G (Addgene plasmid #12259), along with the pLentiPGK Puro DEST ERKKTRClover [a kind gift from Markus Covert; Addgene plasmid #90227 (22)], pLenti-RhoA-2G [a gift from Olivier Pertz; Addgene plasmid #40179 (37)] transfer plasmids, using Lipofectamine 3000 (ThermoFisher) in OptiMEM (Gibco, 21985070), as per the manufacturer's protocol. After 24 h, the media were changed for complete growth medium and incubated for a further 24 h, at which point the media were collected and filtered through a 0.45 μm syringe filter. Cells were then transduced with lentivirus for 48 h in the presence of polybrene (8 μg/mL; Sigma, TR-1003-G) before washing and selection of stable positive cells using puromycin (2 μg/mL). Cells were then sorted by fluorescence-activated cell sorting to isolate a population within a similar fluorescence range.

Live imaging of KTR Cells. A total of 2,000 KTR-expressing TIF cells were seeded in 8-well dishes (Ibidi, 80827) and incubated overnight prior to imaging with SiR-DNA (1 μM; Spirochrome, sc007) to mark the nuclei. Imaging was performed using a Zeiss 3i CSU-W1 spinning disk confocal microscope with SlideBook 6 acquisition software and a Zeiss 20x Plan-Apochromat 0.8 NA air objective. Live imaging conditions were achieved with an Okolab bold line heating system at 37 °C, 20% O_2, and 5% CO_2, acquiring images every 3 min for 75 min, treating with DMSO or trametinib (GSK1120212; 1 μM; Selleckchem, S2673) after first imaging for 15 min.

Molecular Cloning. To generate the pENTR221-mTFP1(cp227) construct, mTFP1(cp227) was PCR amplified from the pLenti-Rac1-2G plasmid [a gift from Olivier Pertz; Addgene plasmid #66111 (69)] to add flanking attB1/attB2 sites using the mTFP1_attB1_F: 5′-TAGAACAAGTTTGTACAAAAAAGCAGGCTCAGCCACC ATGGCACACCATCACCACCATCACG-3′ and mTFP1_attB2_R: 5′-TAGGGACCACTTTGT ACAAGAAAGCTGGGTAGCGTCCGGAGTTGCGGGCCAC-3′ primers. This PCR fragment was then BP subcloned with pDONR221 (ThermoFisher, 12536-017) using BP clonase II (ThermoFisher, 11789), as per the manufacturer's instructions, to yield pENTR221-mTFP1(cp227). The mScarlet (70) fragment was ordered as a gBlock gene fragment from IDT with flanking XhoI/BamHI sites to allow ligation into the pENTR2b (A10463, ThermoFisher) vector to generate pENTR2b-mScarlet (Addgene plasmid #207961), after both were digested with XhoI (ThermoFisher, FD0694) and BamHI (ThermoFisher, FD0054). These vectors then facilitated LR subcloning with pEF.DEST51 (ThermoFisher, 12285-011) using LR clonase II (ThermoFisher, 11791), as per the manufacturer's instructions, to generate pEF.DEST51-mTFP1(cp227) and pEF.DEST51-mScarlet (Addgene plasmid #207960). Similarly, pENTR221-ARHGEF2 was LR subcloned with pDEST-N-term_mCherry (a kind gift from Maria Vartiainen, University of Helsinki, Helsinki, Finland) to generate pDEST-mCherry-ARHGEF2 (Addgene plasmid #207959).

Statistical Analysis. All statistical comparisons were performed using Prism 7 (GraphPad software), as indicated in the figure legends, repeating all experiments at least three times independently. PCA was performed in RStudio using the factoextra package, while robust z-scores were calculated using the stats package.

Stochastic Computational Model of Cell Spreading. The spreading of cells on soft elastic substrates was modeled using a previously described MATLAB implementation of the 2D whole-cell model for spreading and motility (cell migration simulator; CMS) developed by Odde and colleagues (44). The method uses Gillespie Stochastic Simulation Algorithm (71) to model an entire cell by connecting several molecular motor-clutch modules to a central cell body and balancing the resulting forces at the center. The detailed algorithms and equations governing the base CMS have been reported in full previously (44). Here, we added a previously described maximum limit of 100 s^{-1} on the effective clutch off-rate $k_{off,i}$ to increase the simulation efficiency (46). See *SI Appendix*, *Extended Methods* and *SI Appendix*, Table S1 for more information on the model and its parameters.

Individual cells were simulated for 60 min (in-simulation) to allow the system to reach a dynamic steady state, after which the simulation was continued for 4 h and the results were recorded. The average surface areas covered by each cell and the average numbers of engaged clutches during the course of the simulation were calculated and reported.

The CMS was run using MATLAB R2021a with the following toolboxes: Optimization, Mapping, Image Processing, Curve Fitting, and Parallel Computing. Simulation results were visualized using a custom MATLAB script, based on the definition of cell mask in the original CMS.

Data, Materials, and Software Availability. All study data are included in the article and supporting information. The CMS code is available online on the Odde lab website (https://oddelab.umn.edu/) (44), while the custom MATLAB script for visualizing CMS output is available via GitHub (https://github.com/Ivaska-Lab-UTU/CellMigrationSimulator) (72).

ACKNOWLEDGMENTS. We thank P. Laasola and J. Siivonen for technical assistance and the Ivaska lab for scientific discussion and feedback on the manuscript. For critical reading and editing, we thank Dr. Hellyeh Hamidi. For services, instrumentation, and expertise at Turku Bioscience (University of Turku, Turku, Finland), we would like to thank the Cell Imaging and Cytometry Core and the Genome Editing core, which are supported by Biocenter Finland. The clone pENTR221-ARHGEF2 was from the ORFeome library at the Genome Biology Unit core facility, supported by HiLIFE and the Faculty of Medicine, University of Helsinki, and Biocenter Finland. This work was supported by the Finnish Cancer Institute (K. Albin Johansson Professorship to J.I.); a Research Council of Finland research project (grant no. 325464 to J.I.) and Centre of Excellence program (grant no. 346131 to J.I.); the Cancer Foundation Finland (to J.I.); the Sigrid Juselius Foundation (to J.I.); and the Research Council of Finland InFLAMES Flagship program (grant no. 337530 and 357910). J.R.W.C. was supported by the European Union's Horizon 2020 research and innovation program under the Marie Sklodowska-Curie grant agreement (841973) and a Research Council of

Finland postdoctoral research grant (338585). G.F. was supported by a Research Council of Finland postdoctoral research grant (332402). A.I. was supported by the Finnish Cultural Foundation (00210428), the Orion Research Foundation, and the K. Albin Johansson's Foundation. N.P. was supported by the "PhD in Oncology" program of the Philantropia Foundation.

Author affiliations: [a]Turku Bioscience Centre, University of Turku and Åbo Akademi University, Turku FI-20520, Finland; [b]Misvik Biology Oy, Turku FI-20520, Finland; [c]Department of Oncology and Metabolism, University of Sheffield, Sheffield S10 2TN, United Kingdom; [d]Department of Life Technologies, University of Turku, Turku FI-20520, Finland; [e]InFLAMES Research Flagship, University of Turku, Turku FI-20520, Finland; [f]Western Finnish Cancer Center, University of Turku, Turku FI-20520, Finland; and [g]Foundation for the Finnish Cancer Institute, Helsinki FI-00014, Finland

1. H. Hamidi, J. Ivaska, Every step of the way: Integrins in cancer progression and metastasis. *Nat. Rev. Cancer* **18**, 533–548 (2018), 10.1038/s41568-018-0038-z.
2. J. R. W. Conway, G. Jacquemet, Cell matrix adhesion in cell migration. *Essays Biochem.* **63**, 535–551 (2019).
3. S. McFarlane, C. McFarlane, N. Montgomery, A. Hill, D. J. Waugh, CD44-mediated activation of alpha5beta1-integrin, cortactin and paxillin signaling underpins adhesion of basal-like breast cancer cells to endothelium and fibronectin-enriched matrices. *Oncotarget* **6**, 36762–36773 (2015).
4. R. Kaukonen *et al.*, Normal stroma suppresses cancer cell proliferation via mechanosensitive regulation of JMJD1a-mediated transcription. *Nat. Commun.* **7**, 12237 (2016).
5. V. Izzi *et al.*, Pan-cancer analysis of the expression and regulation of matrisome genes across 32 tumor types. *Matrix Biol. Plus* **1**, 100004 (2019).
6. J. R. Mao, J. Bristow, The Ehlers-Danlos syndrome: On beyond collagens. *J. Clin. Invest.* **107**, 1063–1069 (2001).
7. J. F. Bateman, R. P. Boot-Handford, S. R. Lamande, Genetic diseases of connective tissues: Cellular and extracellular effects of ECM mutations. *Nat. Rev. Genet.* **10**, 173–183 (2009).
8. A. L. Wishart *et al.*, Decellularized extracellular matrix scaffolds identify full-length collagen VI as a driver of breast cancer cell invasion in obesity and metastasis. *Sci. Adv.* **6**, eabc3175 (2020).
9. A. Ishihara, T. Yoshida, H. Tamaki, T. Sakakura, Tenascin expression in cancer cells and stroma of human breast cancer and its prognostic significance. *Clin. Cancer Res.* **1**, 1035–1041 (1995).
10. B. Fernandez-Garcia *et al.*, Expression and prognostic significance of fibronectin and matrix metalloproteases in breast cancer metastasis. *Histopathology* **64**, 512–522 (2014).
11. C. J. Flaim, S. Chien, S. N. Bhatia, An extracellular matrix microarray for probing cellular differentiation. *Nat. Methods* **2**, 119–125 (2005).
12. M. Ahmed *et al.*, Combinatorial ECM arrays identify cooperative roles for matricellular proteins in enhancing the generation of TH+ neurons from human pluripotent cells. *Front. Cell Dev. Biol.* **9**, 755406 (2021).
13. A. Brougham-Cook *et al.*, High throughput interrogation of human liver stellate cells reveals microenvironmental regulation of phenotype. *Acta Biomater.* **138**, 240–253 (2022).
14. N. E. Reticker-Flynn *et al.*, A combinatorial extracellular matrix platform identifies cell-extracellular matrix interactions that correlate with metastasis. *Nat. Commun.* **3**, 1122 (2012).
15. T. Pellinen *et al.*, A functional genetic screen reveals new regulators of beta1-integrin activity. *J. Cell Sci.* **125**, 649–661 (2012).
16. C. F. Guimarães, L. Gasperini, A. P. Marques, R. L. Reis, The stiffness of living tissues and its implications for tissue engineering. *Nat. Rev. Mater.* **5**, 351–370 (2020).
17. I. Acerbi *et al.*, Human breast cancer invasion and aggression correlates with ECM stiffening and immune cell infiltration. *Integr. Biol. (Camb)* **7**, 1120–1134 (2015).
18. B. Piersma, M. K. Hayward, V. M. Weaver, Fibrosis and cancer: A strained relationship. *Biochim. Biophys. Acta Rev. Cancer* **1873**, 188356 (2020).
19. A. E. Mayorca-Guiliani *et al.*, ISDoT: In situ decellularization of tissues for high-resolution imaging and proteomic analysis of native extracellular matrix. *Nat. Med.* **23**, 890–898 (2017).
20. S. J. Heo *et al.*, Aberrant chromatin reorganization in cells from diseased fibrous connective tissue in response to altered chemomechanical cues. *Nat. Biomed. Eng.* **7**, 177–191 (2022), 10.1038/s41551-022-00910-5.
21. M. Papanicolaou *et al.*, Temporal profiling of the breast tumour microenvironment reveals collagen XII as a driver of metastasis. *Nat. Commun.* **13**, 4587 (2022).
22. T. Kudo *et al.*, Live-cell measurements of kinase activity in single cells using translocation reporters. *Nat. Protocols* **13**, 155 (2017).
23. K. L. Yee, V. M. Weaver, D. A. Hammer, Integrin-mediated signalling through the MAP-kinase pathway. *IET Syst. Biol.* **2**, 8–15 (2008).
24. A. E. Aplin, S. A. Stewart, R. K. Assoian, R. L. Juliano, Integrin-mediated adhesion regulates ERK nuclear translocation and phosphorylation of Elk-1. *J. Cell Biol.* **153**, 273–282 (2001).
25. M. Aragona *et al.*, A mechanical checkpoint controls multicellular growth through YAP/TAZ regulation by actin-processing factors. *Cell* **154**, 1047–1059 (2013).
26. T. Panciera, L. Azzolin, M. Cordenonsi, S. Piccolo, Mechanobiology of YAP and TAZ in physiology and disease. *Nat. Rev. Mol. Cell Biol.* **18**, 758–770 (2017).
27. S. Dupont *et al.*, Role of YAP/TAZ in mechanotransduction. *Nature* **474**, 179–183 (2011).
28. C. G. Galbraith, K. M. Yamada, M. P. Sheetz, The relationship between force and focal complex development. *J. Cell Biol.* **159**, 695–705 (2002).
29. A. Elosegui-Artola *et al.*, Force triggers YAP nuclear entry by regulating transport across nuclear pores. *Cell* **171**, 1397–1410.e14 (2017).
30. A. Elosegui-Artola *et al.*, Rigidity sensing and adaptation through regulation of integrin types. *Nat. Mater.* **13**, 631–637 (2014).
31. C. D. Lawson, K. Burridge, The on-off relationship of Rho and Rac during integrin-mediated adhesion and cell migration. *Small GTPases* **5**, e27958 (2014).
32. R. G. Hodge, A. J. Ridley, Regulating Rho GTPases and their regulators. *Nat. Rev. Mol. Cell Biol.* **17**, 496–510 (2016).
33. J. Hu, X. Gong, S. Stromblad, Local temporal Rac1-GTP nadirs and peaks restrict cell protrusions and retractions. *Sci. Adv.* **8**, eabl3667 (2022).
34. H. Warner, B. J. Wilson, P. T. Caswell, Control of adhesion and protrusion in cell migration by Rho GTPases. *Curr. Opin. Cell Biol.* **56**, 64–70 (2019).
35. M. Machacek *et al.*, Coordination of Rho GTPase activities during cell protrusion. *Nature* **461**, 99–103 (2009).
36. S. Seetharaman *et al.*, Microtubules tune mechanosensitive cell responses. *Nat. Mater.* **21**, 366–377 (2022).
37. R. D. Fritz *et al.*, A versatile toolkit to produce sensitive FRET biosensors to visualize signaling in time and space. *Sci. Signal.* **6**, rs12 (2013).
38. A. Tao *et al.*, Identifying constitutive and context-specific molecular-tension-sensitive protein recruitment within focal adhesions. *Dev. Cell* **58**, 522–534.e7 (2023).
39. K. Legerstee, B. Geverts, J. A. Slotman, A. B. Houtsmuller, Dynamics and distribution of paxillin, vinculin, zyxin and VASP depend on focal adhesion location and orientation. *Sci. Rep.* **9**, 10460 (2019).
40. J. C. Friedland, M. H. Lee, D. Boettiger, Mechanically activated integrin switch controls alpha5beta1 function. *Science* **323**, 642–644 (2009).
41. P. Atherton *et al.*, Vinculin controls talin engagement with the actomyosin machinery. *Nat. Commun.* **6**, 10038 (2015).
42. J. S. Cheah *et al.*, Spatial proximity of proteins surrounding zyxin under force-bearing conditions. *Mol. Biol. Cell* **32**, 1221–1228 (2021).
43. M. S. Schmitt *et al.*, Zyxin is all you need: Machine learning adherent cell mechanics. ArXiv [Preprint] (2023). https://doi.org/10.48550/arXiv.2303.00176 (Accessed 1 March 2023).
44. B. L. Bangasser *et al.*, Shifting the optimal stiffness for cell migration. *Nat. Commun.* **8**, 15313 (2017).
45. C. E. Chan, D. J. Odde, Traction dynamics of filopodia on compliant substrates. *Science* **322**, 1687–1691 (2008).
46. A. Isomursu *et al.*, Directed cell migration towards softer environments. *Nat. Mater.* **21**, 1081–1090 (2022), 10.1038/s41563-022-01294-2.
47. B. L. Bangasser, S. S. Rosenfeld, D. J. Odde, Determinants of maximal force transmission in a motor-clutch model of cell traction in a compliant microenvironment. *Biophys. J.* **105**, 581–592 (2013).
48. A. Elosegui-Artola *et al.*, Mechanical regulation of a molecular clutch defines force transmission and transduction in response to matrix rigidity. *Nat. Cell Biol.* **18**, 540–548 (2016).
49. Y. Su *et al.*, Relating conformation to function in integrin alpha5beta1. *Proc. Natl. Acad. Sci. U.S.A.* **113**, E3872–E3881 (2016).
50. A. Byron *et al.*, Anti-integrin monoclonal antibodies. *J. Cell Sci.* **122**, 4009–4011 (2009).
51. H. B. Schiller *et al.*, beta1- and alphav-class integrins cooperate to regulate myosin II during rigidity sensing of fibronectin-based microenvironments. *Nat. Cell Biol.* **15**, 625–636 (2013).
52. J. Li, J. Yan, T. A. Springer, Low-affinity integrin states have faster ligand-binding kinetics than the high-affinity state. *Elife* **10**, e73359 (2021).
53. M. Tulla *et al.*, Selective binding of collagen subtypes by integrin alpha 1I, alpha 2I, and alpha 10I domains. *J. Biol. Chem.* **276**, 48206–48212 (2001).
54. C. F. Tiger, F. Fougerousse, G. Grundstrom, T. Velling, D. Gullberg, Alpha11beta1 integrin is a receptor for interstitial collagens involved in cell migration and collagen reorganization on mesenchymal nonmuscle cells. *Dev. Biol.* **237**, 116–129 (2001).
55. M. Lerche *et al.*, Integrin binding dynamics modulate ligand-specific mechanosensing in mammary gland fibroblasts. *iScience* **23**, 100907 (2020).
56. M. Yamada, K. Sekiguchi, Molecular basis of laminin-integrin interactions. *Curr. Top Membr.* **76**, 197–229 (2015).
57. J. R. W. Conway, N. O. Carragher, P. Timpson, Developments in preclinical cancer imaging: Innovating the discovery of therapeutics. *Nat. Rev. Cancer* **14**, 314–328 (2014).
58. R. Straussman *et al.*, Tumour micro-environment elicits innate resistance to RAF inhibitors through HGF secretion. *Nature* **487**, 500–504 (2012).
59. K. R. Levental *et al.*, Matrix crosslinking forces tumor progression by enhancing integrin signaling. *Cell* **139**, 891–906 (2009).
60. K. J. Murphy *et al.*, Intravital imaging technology guides FAK-mediated priming in pancreatic cancer precision medicine according to Merlin status. *Sci. Adv.* **7**, eabh0363 (2021).
61. A. P. Drain *et al.*, Matrix compliance permits NF-kappaB activation to drive therapy resistance in breast cancer. *J. Exp. Med.* **218**, e20191360 (2021).
62. G. Bianchini *et al.*, Molecular anatomy of breast cancer stroma and its prognostic value in estrogen receptor-positive and -negative cancers. *J. Clin. Oncol.* **28**, 4316–4323 (2010).
63. H. Y. Chang *et al.*, Robustness, scalability, and integration of a wound-response gene expression signature in predicting breast cancer survival. *Proc. Natl. Acad. Sci. U.S.A.* **102**, 3738–3743 (2005).
64. A. Planche *et al.*, Identification of prognostic molecular features in the reactive stroma of human breast and prostate cancer. *PLoS One* **6**, e18640 (2011).
65. G. Finak *et al.*, Stromal gene expression predicts clinical outcome in breast cancer. *Nat. Med.* **14**, 518–527 (2008).
66. J. J. Lee *et al.*, Stromal response to Hedgehog signaling restrains pancreatic cancer progression. *Proc. Natl. Acad. Sci. U.S.A.* **111**, E3091–E3100 (2014).
67. N. Barber-Perez *et al.*, Mechano-responsiveness of fibrillar adhesions on stiffness-gradient gels. *J. Cell Sci.* **133**, jcs242909 (2020).
68. G. Chen *et al.*, Chemically defined conditions for human iPSC derivation and culture. *Nat. Methods* **8**, 424–429 (2011).
69. R. D. Fritz *et al.*, SrGAP2-dependent integration of membrane geometry and slit-robo-repulsive cues regulates fibroblast contact inhibition of locomotion. *Dev. Cell* **35**, 78–92 (2015).
70. D. S. Bindels *et al.*, mScarlet: A bright monomeric red fluorescent protein for cellular imaging. *Nat. Methods* **14**, 53–56 (2017).
71. D. T. Gillespie, Exact stochastic simulation of coupled chemical reactions. *J. Phys. Chem.* **81**, 2340–2361 (1977).
72. J. R. W. Conway *et al.*, Ivaska-Lab-UTU/CellMigrationSimulator. GitHub. https://github.com/Ivaska-Lab-UTU/CellMigrationSimulator. Deposited 9 February 2023.